

# Super-Resolution ISAR Imaging Using the Off-the-Grid Structured Low-Rank Method

Bangjie Zhang<sup>1</sup>, Student Member, IEEE, Gang Xu<sup>2</sup>, Senior Member, IEEE, Xiang-Gen Xia<sup>3</sup>, Fellow, IEEE, Hanwen Yu<sup>4</sup>, Senior Member, IEEE, Mengdao Xing, Fellow, IEEE, and Wei Hong<sup>5</sup>, Fellow, IEEE

**Abstract**—Inverse synthetic aperture radar (ISAR) imaging relies on wideband waveform and viewing angle variation to achieve range and cross-range resolutions, respectively. To enhance the resolutions of 2-D images, sparse signal-processing techniques, such as compressed sensing (CS), have been applied to ISAR imaging using a sparse prior. Despite its efficiency in super-resolution imaging, the performance of CS is constrained due to the mismatch of the discrete dictionary, such as the Fourier transform. To address this issue, we propose a novel off-the-grid super-resolution ISAR imaging algorithm that employs a structured low-rank approach to effectively extrapolate the data bandwidth and aperture. To fully capture the low-rank property of ISAR data, the structured data model is constructed and its low-rank property is deduced to exhibit that the signal is embedded in a limited dimensional subspace. Then, the annihilating filter is derived by constructing a structured data matrix to formulate the proposed structured low-rank method, termed as off-the-grid super-resolution using annihilation constraint (OSAC). Taking into account that super-resolution imaging is highly reliant on the accuracy of the annihilating filter, the optimal annihilating filter is also estimated with the updating of extrapolated ISAR data. Through iterative updates of the annihilating filter and solution of the minimization problem, super-resolution ISAR imaging can be achieved by avoiding the discrete mismatch of the conventional CS method. Due to the effective exploration of structured low-rank property, the proposed OSAC algorithm offers superior precision in scatterer location and structure interpretation of a target. Experimental results using both simulated and real data are presented to verify the enhanced performance of 2-D resolution in ISAR imaging.

**Index Terms**—Annihilating filter, inverse synthetic aperture radar (ISAR), off-the-grid compressed sensing (CS), super-resolution.

Received 27 March 2024; revised 6 October 2024; accepted 1 November 2024. Date of publication 12 November 2024; date of current version 17 January 2025. This work was supported in part by the National Science Foundation of China (NSFC) under Grant 62071113, in part by the Natural Science Foundation of Jiangsu Province under Grant BK20211559, and in part by the Fundamental Research Funds for the Central Universities under Grant 2242022k60008 and Grant 2242022R40008. (Corresponding author: Gang Xu.)

Bangjie Zhang, Gang Xu, and Wei Hong are with the State Key Laboratory of Millimeter Waves, School of Information Science and Engineering, Southeast University, Nanjing 210096, China (e-mail: gangxu@seu.edu.cn).

Xiang-Gen Xia is with the Department of Electrical and Computer Engineering, University of Delaware, Newark, DE 19716, USA.

Hanwen Yu is with the School of Resources and Environment, University of Electronic Science and Technology of China, Chengdu 611731, China.

Mengdao Xing is with the National Laboratory of Radar Signal Processing, Xidian University, Xi'an 710071, China (e-mail: xmd@xidian.edu.cn).

Digital Object Identifier 10.1109/TAP.2024.3492503

0018-926X © 2024 IEEE. Personal use is permitted, but republication/redistribution requires IEEE permission. See <https://www.ieee.org/publications/rights/index.html> for more information.

## NOMENCLATURE

$x, \mathbf{x}, \mathbf{X}$	Scalar, vector, matrix.
$\bar{\mathbf{X}}, \mathbf{X}^T, \mathbf{X}^H$	Conjugate, transpose, conjugate transpose of $\mathbf{X}$ .
$\mathbf{X}(M_1 : M_2, :)$	$M_1$ to $M_2$ rows and all the columns of $\mathbf{X}$ .
$\mathbf{X}(:, N_1 : N_2)$	$N_1$ to $N_2$ columns and all the rows of $\mathbf{X}$ .
$\ \mathbf{x}\ _p, \ \mathbf{X}\ _F,  \mathbf{X} $	$l_p$ -norm of $\mathbf{x}$ , Frobenius norm of $\mathbf{X}$ , amplitude of each element of $\mathbf{X}$ .
$\otimes, \odot$ and $*$	Kronecker product, Hadamard product and convolution operation.
$\lfloor \cdot \rfloor, \lceil \cdot \rceil$	Round down to the nearest integer, round up to the nearest integer.
$\mathbf{x} = \text{vec}(\mathbf{X})$	Vectorization by sequentially concatenating the columns of $\mathbf{X}$ .
$\mathbf{X} = \text{reshape}(\mathbf{x}, M, N)$	Reshape $\mathbf{x} \in \mathbb{C}^{MN \times 1}$ into $\mathbf{X} \in \mathbb{C}^{M \times N}$ with $\mathbf{X}(m, n) = \mathbf{x}((n-1)*M + m)$ .
$\mathcal{F}(\mathbf{x}), \mathcal{F}^\dagger(\mathbf{X})$	2-D fast Fourier transform (FFT), 2-D inverse fast Fourier transform (IFFT).

## I. INTRODUCTION

AS AN active microwave sensing tool for moving targets, inverse synthetic aperture radar (ISAR) has found wide applications in both civil and military fields [1], [2], [3], [4], [5]. Basically, the 2-D resolutions in range and cross-range are achieved by the transmitting wideband signal and viewing angle variation, respectively [6]. The range resolution is inversely proportional to the bandwidth of the transmitted signal, and the bandwidth is determined by the capability of the radar system. Meanwhile, the cross-range resolution is related to the rotational angle of the target using the conventional ISAR imaging algorithm, such as the range-Doppler (RD) algorithm, where increasing the coherent processing interval (CPI) generally contributes to resolution refinement. Nevertheless, it may be hard to achieve wideband waveform and long CPI observation in some practical applications. First, wideband waveforms are more susceptible to interference in complex electromagnetic environments. It is a good choice for radar systems to reduce the waveform bandwidth due to the requirement of anti-jamming. Second, it is challenging to perform long coherent processing of maneuvering targets for high-resolution imaging. When the target does not meet the assumption of relatively stable motion during CPI,

ISAR images will become defocused, greatly affecting image quality. In these cases, only narrowband and short aperture observation of the target is available, which will result in limited 2-D resolutions of the image according to the ISAR principles and the Rayleigh criterion [8]. The concept of super-resolution originates from the signal-processing community, called super-resolution spectrum estimation by using a limited number of data [9]. For radar imaging applications, the task of utilizing smaller bandwidth and shorter aperture radar to achieve comparable imaging performance as a wider bandwidth and longer aperture radar has become a research topic in the radar community and is referred to as super-resolution imaging [10], [11].

For super-resolution ISAR imaging, a variety of methods have been proposed [11], [12], [13], [14], [15], [16], [17], [18], [19], [20], [21], including conventional spectrum estimation methods and compressed sensing (CS) methods. The BURGL algorithm, which employs a linear prediction model to fit radar echo and extrapolate data, is a representative algorithm and has been used for super-resolution ISAR imaging [13]. Other classical spectrum estimation algorithms, such as RELAX [14], iterative adaptive approach (IAA) [15], [16], and multiple signal classification (MUSIC) [17], have also been utilized for super-resolution imaging. With the development of CS, sparse ISAR imaging algorithms based on CS technology have emerged, which can be categorized as greedy, convex relaxation, sparse Bayesian learning (SBL), and so on. Orthogonal matching pursuit (OMP) is actually a typical greedy algorithm, which finds possible solutions one by one from the atoms [18]. As the greedy algorithms find the finite dominant scattering points one by one, the derived imaging results are composed of multiple fragmentary points, which may potentially cause the loss of target structure information. Another kind of algorithm, convex relaxation, relaxes the NP-hard problem with the original  $l_0$ -norm constraint to a convex optimization problem with the  $l_p$ -norm ( $0 < p \leq 1$ ) constraint [19], [20]. From the perspective of the inverse problem, the relaxed imaging model is transformed into an underdetermined problem with sparse constraints. Another way, SBL, handles the sparse imaging problem from the perspective of statistical modeling. The probability density function (pdf) is made using a statistical hierarchical model in SBL algorithms, and Laplace distribution is widely adopted to enforce sparseness on the ISAR image [21], [22]. Based on the sparse constraint, the hyperparameter of the hierarchical model is controlled to follow the Laplace distribution for the sparse signal.

In essence, the aforementioned algorithms for super-resolution ISAR imaging are grounded in the sparsity of scattering points in ISAR images. This implies that the majority of these algorithms model the target as a collection of discrete points, often overlooking the structural information of the target. However, it is recognized that while the scattering point model is widely employed, the interpoint correlation can also provide valuable insights into the structure of the target. Algorithms that leverage local structural prior of joint sparsity [23], correlated prior that statistically maintains the continuity of scattering points [24] and pattern-coupled block-sparse prior [25],

[26], [27] have been developed for high-resolution ISAR imaging. In addition, the incorporation of Markov random fields [28], image-domain convolution reweighting [29], and total variation norm (TV-norm) constraint [30] have been explored to encapsulate the continuous structure of the image, thereby refining the image quality.

The CS algorithms have several common characteristics. First, the relationship between the echo and the image is described through a grid dictionary. Second, the imaging process is formulated as an inverse problem, utilizing the dictionary. Moreover, by leveraging prior knowledge in the image domain and integrating it into the inverse problem, super-resolution imaging can be achieved with the help of additional information. The performance of CS is notably restricted by the restricted isometry property (RIP), which imposes a limit on the attainable level of super-resolution. In addition, the basis mismatch that arises from constructing the dictionary is a fundamental issue inherent in gridding-based CS.

To overcome the issue of basis mismatch, off-the-grid technologies have been proposed for gridless CS [31], [32], [33], [34], [35]. Matrix completion (MC) techniques that exploit low-rank [33] and structured low-rank property [34] are prominent examples of gridless CS algorithms, capable of preserving structural information within high-dimensional echo data. Algorithms using low-rank constraints generally model the radar echo to be composed of multiple supporting sets. The incoherence between sets has an evident impact on the performance of MC, akin to the RIP of CS. For sparse ISAR imaging, the performance of low-rank algorithms is sensitive to the sparse sampling of echoes and has a good sparse recovery performance under the case of random sparse sampling. For example, our previous work [34] demonstrated that the performance of the structured low-rank algorithm deteriorated significantly when sparse sampling cases with low randomness were adopted, such as gapped missing sampling. As an alternative to low-rank constraint, atomic norm minimization (ANM) has been introduced for matrix recovery and gridless CS. A new nonconvex optimization model based on the 2-D ANM framework has been proposed in [35] for 2-D gridless sparse ISAR imaging. The reweighted 2-D ANM algorithm can achieve high-resolution ISAR imaging with remarkable computational efficiency.

Generally, the low-rank prior has been extensively employed in the field of sparse imaging. However, to the best of our knowledge, the utilization of low-rank property for super-resolution ISAR imaging has not been previously explored. In this article, a super-resolution ISAR imaging algorithm that harnesses the structured low-rank property is proposed, which is termed as off-the-grid super-resolution using annihilation constraint (OSAC). First, a target component is considered to be residing within a low-dimensional subspace of high-dimensional echo. The complementary subspace, referred to as the annihilating subspace in the following, is orthogonal to the respective target component, analogous to the orthogonality between the signal and noise subspaces in MUSIC. This orthogonality of subspace is known as the annihilating property in the framework of finite rate of innovation (FRI) theory, that is, there is an annihilating filter that sets the signal

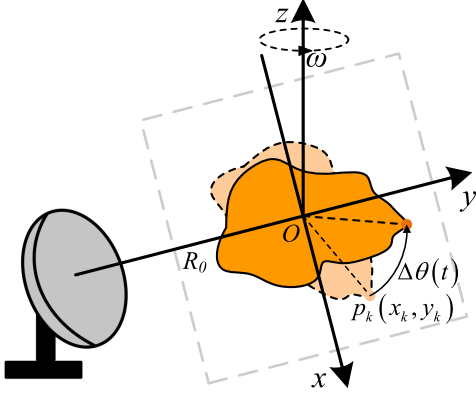


Fig. 1. Turntable model of ISAR imaging.

component zero [36], [37], [38]. To estimate the annihilating subspace, a structured echo matrix is constructed based on low-resolution echo, and singular value decomposition (SVD) is performed. The annihilating filter is then estimated by reweighting and combining the singular vectors corresponding to the smallest singular values. Then, the annihilating property is used as a constraint for the minimization problem. Super-resolution imaging is achieved by updating the annihilating filter and the imaging result iteratively.

The remainder of this article is outlined as follows. First, the basic signal model of ISAR imaging and structured low-rank property of ISAR echo is introduced in Section II. After expounding the connection between structured low-rank property and annihilating property, off-the-grid super-resolution imaging using annihilation constraint is introduced in detail in Section III. Iterative steps of estimating annihilating subspace and solving the minimization problem are detailed as well, together with the connection to gridding-based CS algorithm. Finally, numerical experiments using simulated and measured data are performed to validate the effectiveness of the proposed algorithm.

Notations: The mathematical notations of symbols and operators are summarized in Nomenclature.

## II. LOW-RANK SIGNAL MODEL

As Fig. 1 shows, the ISAR imaging geometry can be explained with the help of a turntable model after compensating the translational motion of the target relative to radar using existing methods [39]. Following the point scattering model, the distance from  $p_k(x_k, y_k)$  at the target to the radar at pulse dwell time  $t$  can be expressed as:

$$R_k(t) = R_0 + y_k \cdot \cos \Delta\theta(t) + x_k \cdot \sin \Delta\theta(t) \quad (1)$$

where  $R_0$  denotes the range from the center of the target to the radar.

Based on the assumption of small aspect-angle variation and uniform rotation,  $\Delta\theta(t)$  can be expressed as  $\Delta\theta(t) = \omega \cdot t$ , where  $\omega$  is the constant angular velocity. Taking into account that  $\Delta\theta(t)$  is usually small, (1) can be simplified as

$$\begin{aligned} R_k(t) &= R_0 + y_k \cdot \cos(\omega \cdot t) + x_k \cdot \sin(\omega \cdot t) \\ &\approx R_0 + y_k + x_k \cdot \omega \cdot t \end{aligned} \quad (2)$$

where  $\cos(\omega \cdot t) \approx 1$  and  $\sin(\omega \cdot t) \approx \omega \cdot t$ . Assuming that the radar transmits a linear frequency-modulated (LFM) signal, the waveform  $u(\tau)$  can be expressed as

$$u(\tau) = \text{rect}\left[\frac{\tau}{T_a}\right] \cdot \exp[j\pi\gamma\tau^2] \quad (3)$$

where  $\text{rect}[\cdot]$  is the rectangular function,  $T_a$  is the pulsewidth,  $\gamma$  is the chirp rate, and  $\tau$  is the fast time. Then, the discrete echo after de-chirping can be written as [29]

$$\begin{aligned} \mathbf{S}(m, n) &= \sum_{k=1}^K \sigma_k \cdot \exp\left[\frac{-j4\pi\gamma \cdot (m-1) \cdot y_k}{f_s \cdot c}\right] \\ &\cdot \exp\left[\frac{-j4\pi f_c \cdot \omega \cdot (n-1) \cdot x_k}{c \cdot \text{PRF}}\right] \end{aligned} \quad (4)$$

where  $\sigma_k$  is the scattering coefficient of the  $k$ th scatterer with coordinate  $(x_k, y_k)$ ,  $c$  is the speed of the electromagnetic wave, and  $f_c$  is the carrier frequency.  $f_s$  is the sampling rate during the pulse, PRF is the pulse repetition frequency (PRF), and  $m$  and  $n$  are indices for the sampled echo in the fast time and slow time, respectively. It should be noted that the residual video phase (RVP) is assumed to have been compensated. In addition, there is assumed to be generally no migration through range cell (MTRC) in the case of short CPI. The detailed procedures of de-chirping and the corresponding signal model can be referred to [10] and [29], and so on and will not be elaborated here for the sake of conciseness.

Recalling (4), the discrete echo can be expressed as

$$\mathbf{S} = \mathbf{A} \cdot \mathbf{\Sigma} \cdot \mathbf{B}^T = \sum_{k=1}^K \sigma_k \cdot \mathbf{a}_k \cdot \mathbf{b}_k^T \quad (5)$$

where

$$\begin{aligned} \mathbf{a}_k(m) &= \exp\left[\frac{-j4\pi\gamma \cdot (m-1) \cdot y_k}{f_s \cdot c}\right] \\ \mathbf{b}_k(n) &= \exp\left[\frac{-j4\pi f_c \cdot \omega \cdot (n-1) \cdot x_k}{c \cdot \text{PRF}}\right] \\ \mathbf{A} &= [\mathbf{a}_1 \quad \mathbf{a}_2 \quad \cdots \quad \mathbf{a}_K] \\ \mathbf{B} &= [\mathbf{b}_1 \quad \mathbf{b}_2 \quad \cdots \quad \mathbf{b}_K] \\ \mathbf{\Sigma} &= \text{diag}([\sigma_1 \quad \sigma_2 \quad \cdots \quad \sigma_K]). \end{aligned} \quad (6)$$

The low-rank property of  $\mathbf{S}$  holds

$$\text{rank}(\mathbf{S}) \leq \text{rank}(\mathbf{\Sigma}) = K. \quad (7)$$

In addition to the low-rank property itself, the structured low-rank property is also an important prior, which can be used for enhanced imaging performance [34]. The structured matrix is defined as  $\mathbf{H}_S = \mathcal{H}(\mathbf{S}) \in \mathbb{C}^{(2P+1)(2Q+1) \times (M-2P)(N-2Q)}$ , where  $\mathcal{H}(\cdot)$  is the structure operation. The detailed definition of  $\mathcal{H}(\cdot)$  is to take patches  $\check{\mathbf{S}}_{p,q} \in \mathbb{C}^{(2P+1) \times (2Q+1)}$  from  $\mathbf{S}$ , turn the patches into vectors and stack them as a new matrix, as shown in Fig. 2

The patch  $\check{\mathbf{S}}_{p,q}$  can be expressed as

$$\begin{aligned} \check{\mathbf{S}}_{p,q} &= \mathbf{S}(p-P : p+P, q-Q : q+Q) = \mathbf{A}_p \cdot \mathbf{\Sigma} \cdot \mathbf{B}_q^T \\ \mathbf{A}_p &= \mathbf{A}(p-P : p+P, :), \mathbf{B}_q = \mathbf{B}(q-Q : q+Q, :) \\ p &\in [P+1, M-P], q \in [Q+1, N-Q]. \end{aligned} \quad (8)$$

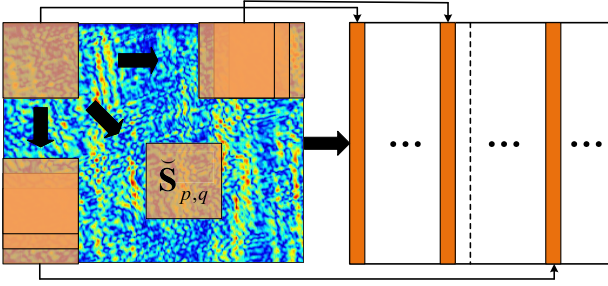


Fig. 2. Construction of the structured matrix.

Providing that

$$\begin{aligned} \mathbf{A}_{p+p'} &= \mathbf{A}_p \cdot \boldsymbol{\Sigma}_{y,p'} \\ \boldsymbol{\Sigma}_{y,p'}(k, k) &= \exp \left[ \frac{-j4\pi\gamma \cdot (p' - 1) \cdot y_k}{f_s \cdot c} \right] \\ \mathbf{B}_{q+q'} &= \mathbf{B}_q \cdot \boldsymbol{\Sigma}_{x,q'} \\ \boldsymbol{\Sigma}_{x,q'}(k, k) &= \exp \left[ \frac{-j4\pi f_c \cdot \omega \cdot (q' - 1) \cdot x_k}{c \cdot \text{PRF}} \right] \end{aligned} \quad (9)$$

and  $\boldsymbol{\Sigma}_{y,p'}$  and  $\boldsymbol{\Sigma}_{x,q'}$  are diagonal matrices, the vectored form can be expressed as

$$\begin{aligned} \mathbf{H}_s(:, p + q) &= \tilde{\mathbf{s}}_{p+p', q+q'} \\ &= (\mathbf{B}_q \otimes \mathbf{A}_p) \cdot \text{vec}(\boldsymbol{\Sigma}_{y,p'} \cdot \boldsymbol{\Sigma} \cdot \boldsymbol{\Sigma}_{x,q'}^T). \end{aligned} \quad (10)$$

Given that  $\boldsymbol{\Sigma}_{y,p'}$ ,  $\boldsymbol{\Sigma}_{x,q'}$ , and  $\boldsymbol{\Sigma}$  are all diagonal matrices, the structured low-rank property of  $\mathbf{H}_s$  holds, which can be expressed as

$$\text{rank}(\mathbf{H}_s) \leq K. \quad (11)$$

### III. OFF-THE-GRID SUPER-RESOLUTION IMAGING USING ANNIHILATION CONSTRAINT

The low-resolution echo  $\mathbf{S}$  corresponds to small bandwidth and short CPI can be considered as downsampled high-resolution echo  $\mathbf{Y}$  in both the fast and slow time, that is,

$$\mathbf{S} = \mathbf{D}_r \cdot \mathbf{Y} \cdot \mathbf{D}_a^T + \mathbf{N} \quad (12)$$

where  $\mathbf{D}_r$  and  $\mathbf{D}_a$  are the downsampling matrix in range and azimuth, the detailed form can be expressed as

$$\begin{aligned} \mathbf{D}_r &= \mathbf{I}_{\tilde{M}} \left( \left\lfloor \frac{\tilde{M}}{2} \right\rfloor - \left\lfloor \frac{M}{2} \right\rfloor + 1 : \left\lceil \frac{\tilde{M}}{2} \right\rceil + \left\lceil \frac{M}{2} \right\rceil, : \right) \\ \mathbf{D}_a &= \mathbf{I}_{\tilde{N}} \left( \left\lfloor \frac{\tilde{N}}{2} \right\rfloor - \left\lfloor \frac{N}{2} \right\rfloor + 1 : \left\lceil \frac{\tilde{N}}{2} \right\rceil + \left\lceil \frac{N}{2} \right\rceil, : \right) \end{aligned} \quad (13)$$

where  $\mathbf{I}_{\tilde{M}} \in \mathbb{R}^{\tilde{M} \times \tilde{M}}$  and  $\mathbf{I}_{\tilde{N}} \in \mathbb{R}^{\tilde{N} \times \tilde{N}}$  are identity matrices with different sizes.  $M$  and  $\tilde{M}$  are the numbers of samplings corresponding to small bandwidth and large bandwidth, respectively.  $N$  and  $\tilde{N}$  are the numbers of pulses corresponding to short CPI and long CPI, respectively.

Recalling (4), when a total number of  $M$  samples are available, the range resolution can be calculated as

$$\delta_r = \frac{f_s \cdot c}{2\gamma M} = \frac{c}{2B} \quad (14)$$

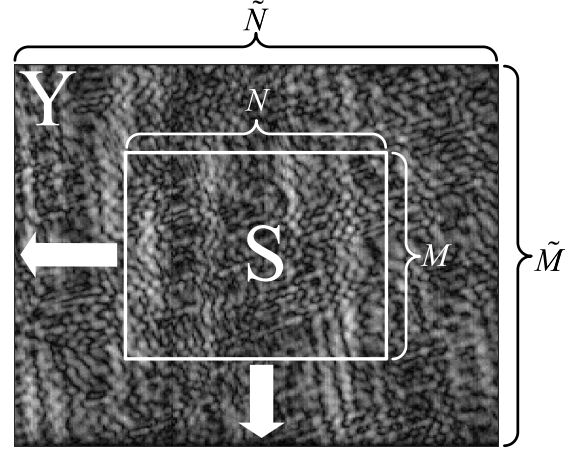


Fig. 3. Illustration of super-resolution imaging by data extrapolation.

where  $B = \gamma \cdot M / f_s$  is the bandwidth of the transmitted signal. Similarly, when a total number of  $N$  pulses are available, the cross-range resolution can be calculated as

$$\delta_a = \frac{c \cdot \text{PRF}}{2f_c \cdot \omega \cdot N} = \frac{\lambda}{2\Delta\theta} \quad (15)$$

where  $\lambda$  is the wavelength corresponding to the carrier frequency and  $\Delta\theta = \omega \cdot N / \text{PRF}$  is the viewing angle variation.

As revealed in (14) and (15), extrapolating an echo contributes to the resolution enhancement. Then, the problem of super-resolution imaging can be converted to a problem of extrapolating  $\mathbf{Y}$  using  $\mathbf{S}$ . For clarity, the relationship between  $\mathbf{Y}$  and  $\mathbf{S}$  is shown in Fig. 3.

In this article, the annihilating property is used and off-the-grid matrix recovery in the data domain is proposed for super-resolution imaging. The annihilating property is derived from the low-rank property, which will be detailed in Section III-A. Then, the off-the-grid super-resolution algorithm containing two steps iteratively is introduced. Unlike the 1-D prediction model in BURG [13], the proposed algorithm utilizes 2-D convolution to extract annihilating property and achieves super-resolution of joint range and cross-range. In addition, the proposed algorithm directly extrapolates the data without relying on the construction of a dictionary in the CS algorithm, which will be analyzed in detail at the end of this section.

#### A. From Low-Rank and Structured Low-Rank to Annihilating

Recalling the proof of low-rank and structured low-rank property in Section II, the signal of the target can be considered to be embedded in a low-dimensional subspace. From another perspective, the signal subspace can be assumed orthogonal to the null space. Annihilating property is used to represent the orthogonality between subspaces in this article, which can be regarded as an extension of structured low-rank property. A detailed analysis is as follows.

1) *Brief Introduction to Annihilating Property:* From the perspective of FRI theory, there exists an annihilating filter  $e(t)$  for signal  $f(t)$  which is composed of finite Diracs in the frequency domain, with the following equation holds

$$e(t) * f(t) = 0. \quad (16)$$



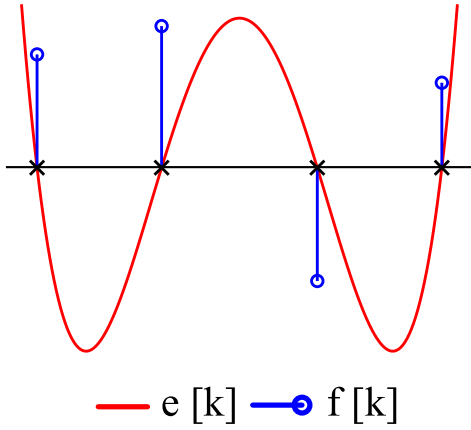


Fig. 4. Illustration of annihilating filter  $e[k]$  for signal  $f[k]$  in the frequency domain.

In other words, the zero points of the annihilating filter  $e[k]$  in the transformed frequency domain coincides with the peaks of  $f[k]$ , as shown in Fig. 4.

2) *Annihilating Property of ISAR Echo*: Enlightened by super-resolution imaging using sparse prior in CS theory, the annihilating property is tried as a prior for resolution enhancement. Furthermore, the annihilating property is extended from Diracs to 2-D ISAR echo by exploiting subspace orthogonality. To avoid basis mismatch, a convolution relationship is used since ISAR echo and image are pairs using Fourier transform in the case of small bandwidth and short aperture. To be more specific, there exists an annihilating filter, denoted as  $\mathbf{E}$ , that satisfies the following relationship:

$$\mathbf{E} * \mathbf{Y} = 0. \quad (17)$$

According to (17), the 2-D convolution  $\mathbf{E} * \mathbf{Y}$  can be rewritten as multiplication  $\mathbf{e}^T \cdot \mathbf{H}_Y$ , where  $\mathbf{e} = \text{vec}(\mathbf{E})$ . When the size of filter is selected as  $\mathbf{E} \in \mathbb{C}^{(2P+1) \times (2Q+1)}$ , the echo is correspondingly divided into patches  $\check{\mathbf{Y}}_{p,q} \in \mathbb{C}^{(2P+1) \times (2Q+1)}$  to construct  $\mathbf{H}_Y$ , which is exactly the construction of structured matrix introduced in Fig. 2. Since the structured low-rank property has been proved, there should exist null space for  $\mathbf{H}_Y$ , which is consistent with the annihilating filter.

### B. Proposed OSAC Algorithm

With the annihilating property proved, off-the-grid super-resolution imaging can be performed. The initial value is taken as  $\mathbf{Y}^{(0)} = \mathbf{S}$ . Then, the proposed algorithm mainly includes two main steps in each iteration. Taking the  $l$ th iteration as an example, the first step is to estimate the annihilating subspace, which can be stated as

$$\mathbf{e}^{(l)} = \text{vec}(\mathbf{E}^{(l)}) = \mathcal{N}(\mathbf{Y}^{(l)}) \quad (18)$$

where  $\mathcal{N}(\cdot)$  denotes the operation to estimate the annihilating subspace, which will be specifically introduced in the first part of this section.

Suppose that  $\mathbf{E}^{(l)}$  has been well estimated, super-resolution imaging using annihilation constraint can be expressed as

$$\min_{\mathbf{Y}^{(l+1)}} \|\mathbf{E}^{(l)} * \mathbf{Y}^{(l+1)}\|_F^2$$

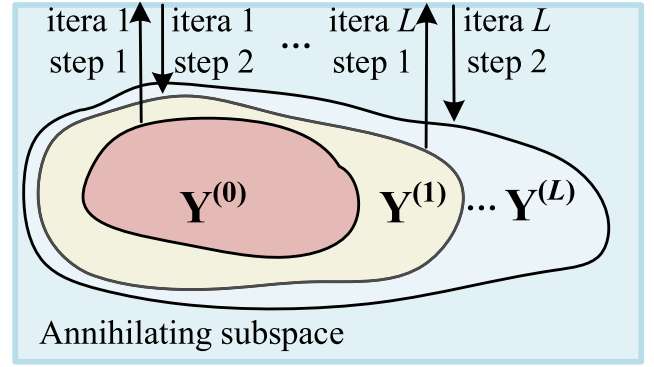


Fig. 5. Procedures of the proposed algorithm.

$$\text{s.t. } \|\mathbf{D}_r \cdot \mathbf{Y}^{(l+1)} \cdot \mathbf{D}_a^T - \mathbf{S}\|_F^2 \leq \epsilon \quad (19)$$

where  $\epsilon$  is the estimated noise power.

Taking into account that the super-resolution imaging is highly dependent on the accuracy of estimation annihilating subspace, two steps are iteratively performed, as shown in Fig. 5. The details are as follows.

1) *Annihilating Subspace Estimation Using Structured Matrix*: The orthogonality between the signal subspace where the signal of the target is embedded and the annihilating subspace is used to evaluate the annihilating subspace, which is similar to that in MUSIC. The following are the detailed steps to estimate the annihilating subspace with low-resolution echo.

First,  $\mathbf{Y}^{(l)}$  is used to construct structured matrix  $\mathbf{H}_Y$ , as shown in Fig. 2. When the patch is selected as  $\check{\mathbf{Y}}_{p,q} = \mathbf{Y}^{(l)}(p-P : p+P, q-Q : q+Q)$ , the relationship between columns of  $\mathbf{H}_Y$  and  $\check{\mathbf{Y}}_{p,q}$  can be expressed as

$$\mathbf{H}_Y(:, (p-P-1)(\tilde{N}-2Q) + q - Q) = \text{vec}(\check{\mathbf{Y}}_{p,q}) \quad (20)$$

where  $p \in [P+1, \tilde{M}-P]$ ,  $q \in [Q+1, \tilde{N}-Q]$ .

Then, SVD  $\mathbf{H}_Y = \mathbf{U}_{H_Y} \cdot \Sigma_{H_Y} \cdot \mathbf{V}_{H_Y}^H$  can be performed. As revealed in (11), the target component is embedded in low-dimensional subspaces corresponding to the  $K$  largest singular values of  $\mathbf{H}_Y$ . That is to say, the annihilating subspaces can be estimated using the minimum singular values. For the  $h$ th singular vector  $\mathbf{u}_{H_Y,h} = \mathbf{U}_{H_Y}(:, h)$ ,  $h \in [K+1, (2P+1)(2Q+1)]$ , the product  $\mathbf{u}_{H_Y,h}^H \cdot \mathbf{H}_Y = \delta_h \cdot \mathbf{v}_{H_Y,h}^H$ , where  $\delta_h$  is the  $h$ th singular value of  $\Sigma_{H_Y}$ . Thus,  $\|\mathbf{u}_{H_Y,h}^H \cdot \mathbf{H}_Y\|_2^2 = \delta_h \cdot \mathbf{v}_{H_Y,h}^H \cdot \mathbf{v}_{H_Y,h} \cdot \delta_h = \delta_h^2$ .

A reweighting strategy is further applied to the subspaces. First, each singular vector is reshaped into the matrix, and 2-D FFT is performed, which is denoted by

$$\mathbf{U}_{H_Y,h} = \mathcal{F}(\text{reshape}(\mathbf{u}_{H_Y,h}, 2P+1, 2Q+1)). \quad (21)$$

Then, the reweighted square root is calculated, which can be expressed as

$$\mathbf{W}(m, n) = \sqrt{\sum_{h=K+1}^{(2P+1)(2Q+1)} \frac{1}{(\delta_h)^\beta} \cdot |\mathbf{U}_{H_Y,h}(m, n)|^2} \quad (22)$$

where  $\beta$  is the exponential which is set to zero in this article. Lastly, the annihilating filter is calculated as

$$\mathbf{E}^{(l)} = \mathcal{F}^\dagger(\mathbf{W}) \quad (23)$$

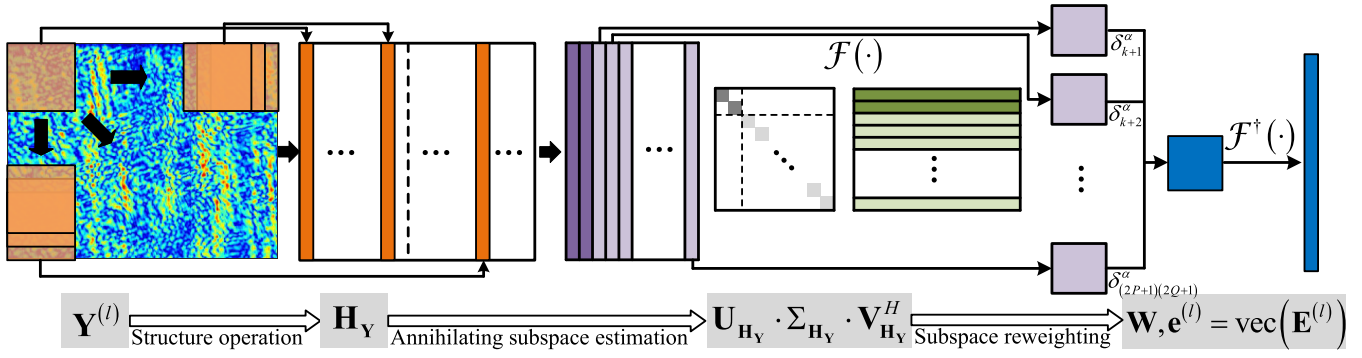


Fig. 6. Procedures of estimating annihilating subspace.

with  $\mathbf{e}^{(l)} = \text{vec}(\mathbf{E}^{(l)})$ . The procedures of estimating annihilating subspace are illustrated in Fig. 6. For the convenience of subsequent expression, annihilating subspace estimation using  $\mathbf{Y}^{(l)}$  is abbreviated as  $\mathbf{e}^{(l)} = \text{vec}(\mathbf{E}^{(l)}) = \mathcal{N}(\mathbf{Y}^{(l)})$ .

2) *Annihilation Constrained Minimization*: After estimating annihilating subspace  $\mathbf{e}^{(l)} = \text{vec}(\mathbf{E}^{(l)})$  in the  $l$ th iteration, (19) in the  $(l+1)$ th iteration can be rewritten as follows:

$$\min_{\mathbf{Y}^{(l+1)}} \|\mathbf{E}^{(l)} * \mathbf{Y}^{(l+1)}\|_F^2 + \lambda \cdot \|\mathbf{D}_r \cdot \mathbf{Y}^{(l+1)} \cdot \mathbf{D}_a^T - \mathbf{S}\|_F^2 \quad (24)$$

where  $\lambda$  is the penalty coefficient. For brief expression, the convolution operation and downsampling operation are rewritten in the form of multiplication since both are linear operations, which can be expressed as

$$\min_{\mathbf{y}^{(l+1)}} \|\mathbf{C}_y^{(l)} \cdot \mathbf{y}^{(l+1)}\|_2^2 + \lambda \cdot \|\mathbf{D} \cdot \mathbf{y}^{(l+1)} - \mathbf{s}\|_2^2 \quad (25)$$

where  $\mathbf{y}$  and  $\mathbf{s}$  are the vector forms of  $\mathbf{Y}$  and  $\mathbf{S}$ , respectively.  $\mathbf{D} = \mathbf{D}_a \otimes \mathbf{D}_r$  is the linear operation corresponding to downsampling.  $\mathbf{C}_y$  corresponds to the convolution operation. It is obvious that (25) has a closed-form solution, which can be stated as

$$\mathbf{y}^{(l+1)} = (\mathbf{C}_y^T \cdot \mathbf{C}_y + \lambda \mathbf{D}^T \cdot \mathbf{D})^{-1} \cdot \lambda \mathbf{D}^T \cdot \mathbf{s}. \quad (26)$$

To avoid inversion of the matrix, (26) can be efficiently solved by the quasi-Newton conjugate gradient (CG) algorithm. The CG is in the following form:

$$\nabla \mathbf{J}(\mathbf{y}^{(l+1)}) = \mathbf{Hess}(\mathbf{y}^{(l+1)}) - \lambda \mathbf{D}^T \cdot \mathbf{S}. \quad (27)$$

It should be noted that  $\mathbf{C}_y$  is exactly taken as a matrix of local convolution with the circular boundary condition, then  $\tilde{\mathbf{C}} = \mathbf{C}_y^T \cdot \mathbf{C}_y$  is a circulant matrix. In this case, the approximated Hessian matrix can be calculated by

$$\mathbf{Hess}(\mathbf{y}^{(l+1)}) = \text{vec}(\mathcal{F}^\dagger(\mathcal{F}(\mathbf{E}^{(l)}) \odot \mathcal{F}(\mathbf{E}^{(l)}) \odot \mathcal{F}(\mathbf{Y}^{(l+1)}))) + \lambda \mathbf{D}^T \cdot \mathbf{D} \cdot \mathbf{y}^{(l+1)} \quad (28)$$

where the convolution property of the circulant matrix in the Fourier domain is utilized. In each iteration, (27) is set to zero using the CG algorithm. In the  $i$ th iteration,  $\mathbf{y}_{(i+1)}^{(l+1)}$  is expressed as

$$\mathbf{y}_{(i+1)}^{(l+1)} = \mathbf{y}_{(i)}^{(l+1)} - \zeta (\mathbf{Hess}(\mathbf{y}_{(i)}^{(l+1)}))^{-1} \cdot \nabla \mathbf{J}(\mathbf{y}_{(i)}^{(l+1)}) \quad (29)$$

where  $\zeta$  is the step size.

The procedure is summarized as Algorithm 1.

#### Algorithm 1 Procedures of OSAC

##### Input:

low-resolution echo  $\mathbf{S}$ ;  $\mathbf{Y}^{(0)} = \mathbf{S}$ ;  
operators  $\mathcal{H}(\cdot)$ ,  $\mathcal{N}(\cdot)$  and  $\mathcal{F}(\cdot)$ ;  
 $\lambda$ ,  $l = 0$ .

- 1: **while** not converge **do**
- 2:    $\mathbf{e}^{(l)} = \mathcal{N}(\mathbf{Y}^{(l)})$
- 3:    $i = 0$
- 4:   **while** not converge **do**
- 5:      $\mathbf{y}_{(i+1)}^{(l+1)} = \mathbf{y}_{(i)}^{(l+1)}$
- 6:      $\quad - \zeta (\mathbf{Hess}(\mathbf{y}_{(i+1)}^{(l+1)}))^{-1} \cdot \nabla \mathbf{J}(\mathbf{y}_{(i+1)}^{(l+1)})$
- 7:      $i = i + 1$
- 8:   **end while**
- 9:    $l = l + 1$
- 10: **end while**

##### Output:

$\mathbf{Y}^{(l+1)}$ .

#### C. Connection to Super-Resolution Using the CS Algorithm

CS can effectively obtain or reconstruct a signal by finding solutions to under-determined linear equations. By introducing sparse prior, the general model of inverse problem can be concluded as

$$\begin{aligned} \min_{\mathbf{x}} \|\mathbf{x}\|_p \\ \text{s.t. } \|\mathbf{s} - \Psi \cdot \mathbf{x}\|_2^2 \leq \epsilon \end{aligned} \quad (30)$$

where  $\|\mathbf{x}\|_p$  with  $0 < p \leq 1$  is the  $l_p$ -norm of  $\mathbf{x}$ ,  $\mathbf{s}$ ,  $\mathbf{x}$ , and  $\Psi$  are the received signal, the image to be solved, and the dictionary matrix, respectively.

In super-resolution, ISAR imaging algorithms using CS, the small bandwidth, and short CPI echo are regarded as downsampled part of echo corresponding to a high-resolution image, which can be expressed as

$$\begin{aligned} \mathbf{S} &= \mathbf{D}_r \cdot \mathbf{Y} \cdot \mathbf{D}_a^T + \mathbf{N} \\ &= \mathbf{D}_r \cdot \mathcal{F}(\mathbf{X}) \cdot \mathbf{D}_a^T + \mathbf{N} \end{aligned} \quad (31)$$

where  $\mathbf{X}$  represents the image to be reconstructed, and  $\mathbf{N}$  is additional Gaussian noise. In data domain, (30) can be written as

$$\begin{aligned} \min_{\mathbf{Y}} \|\text{vec}(\mathcal{F}^\dagger(\mathbf{Y}))\|_p \\ \text{s.t. } \|\mathbf{S} - \mathbf{D}_r \cdot \mathbf{Y} \cdot \mathbf{D}_a^T\|_F^2 \leq \epsilon. \end{aligned} \quad (32)$$

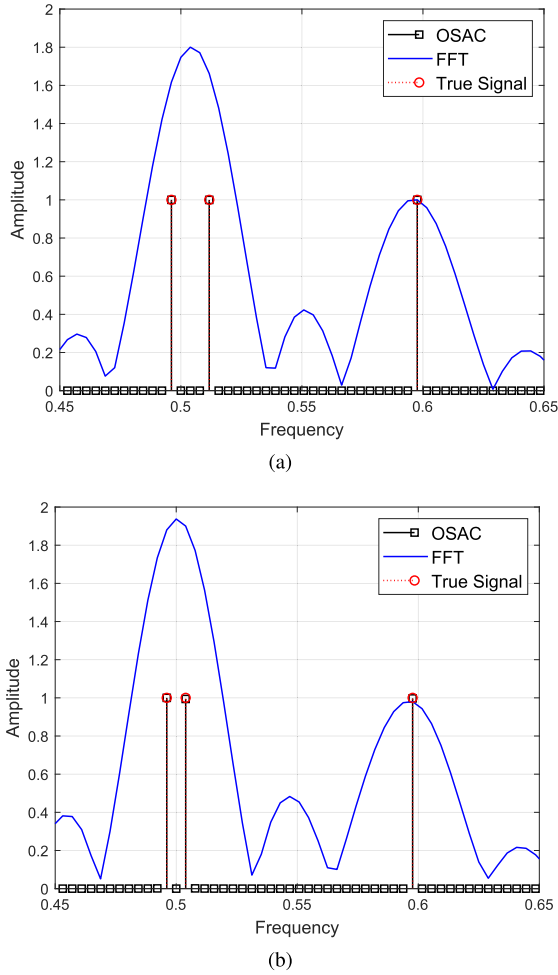


Fig. 7. Line spectrum estimation result. (a) Case of  $\text{SRF} = 2$ . (b) Case of  $\text{SRF} = 4$ .

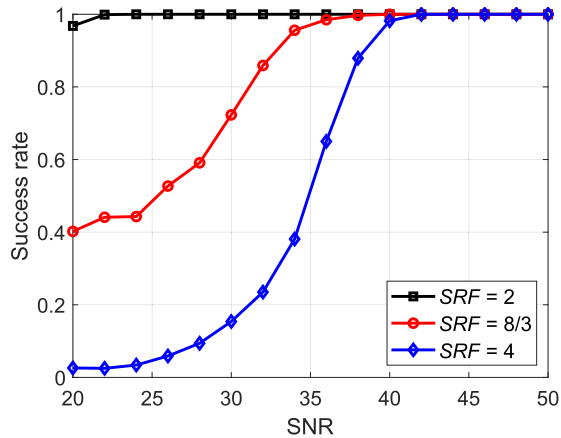


Fig. 8. Success rate of super-resolution versus the SNR and SRF.

As revealed in (32), super-resolution using the CS algorithm can also be regarded as a minimization problem with a constraint. Both algorithms rely on prior information mining to achieve higher resolution. The CS algorithm utilizes a Fourier dictionary to establish the relationship between data and the image, transforming the super-resolution imaging into an ill-posed inverse problem-solving. Each row of the dictionary corresponds to a discrete grid  $\{y, \omega \cdot x\}$  in the image. Differently, the proposed OSAC algorithm utilizes

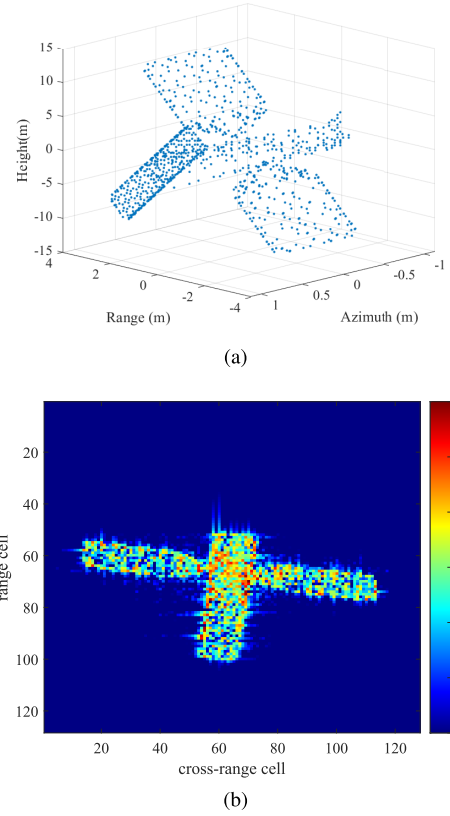


Fig. 9. Model and reference image for the simulated experiment. (a) Model of the satellite. (b) RD image of the satellite.

TABLE I

KEY PARAMETERS OF THE SIMULATED SATELLITE DATASET

System Parameters	Value
Carrier frequency	9.6 GHz
Bandwidth	500 MHz
Coherent processing angle	$3^\circ$
Number of samples per pulse	128
Number of pulses in CPI	128
Range resolution	0.3 m
Cross-range resolution	$\approx 0.29$ m

the annihilating property to directly extrapolate data in the echo domain.

#### IV. EXPERIMENTS

In this section, both simulated and measured data are utilized to validate the performance of the proposed OSAC algorithm. First, simulated experiments of line spectrum estimation are conducted to intuitively demonstrate the super-resolution performance. Then, experiments of ISAR imaging are detailed. The performance is compared with that of algorithms using ANM [35] and improved CS using reweighted  $l_1$ -norm minimization (ICS) [11]. To begin with, a key parameter of the super-resolution factor (SRF) [9] is defined to evaluate the imaging performance. In the experiments of line spectrum estimation, when the spacing of two Diracs is  $1/\tilde{N}$ ,

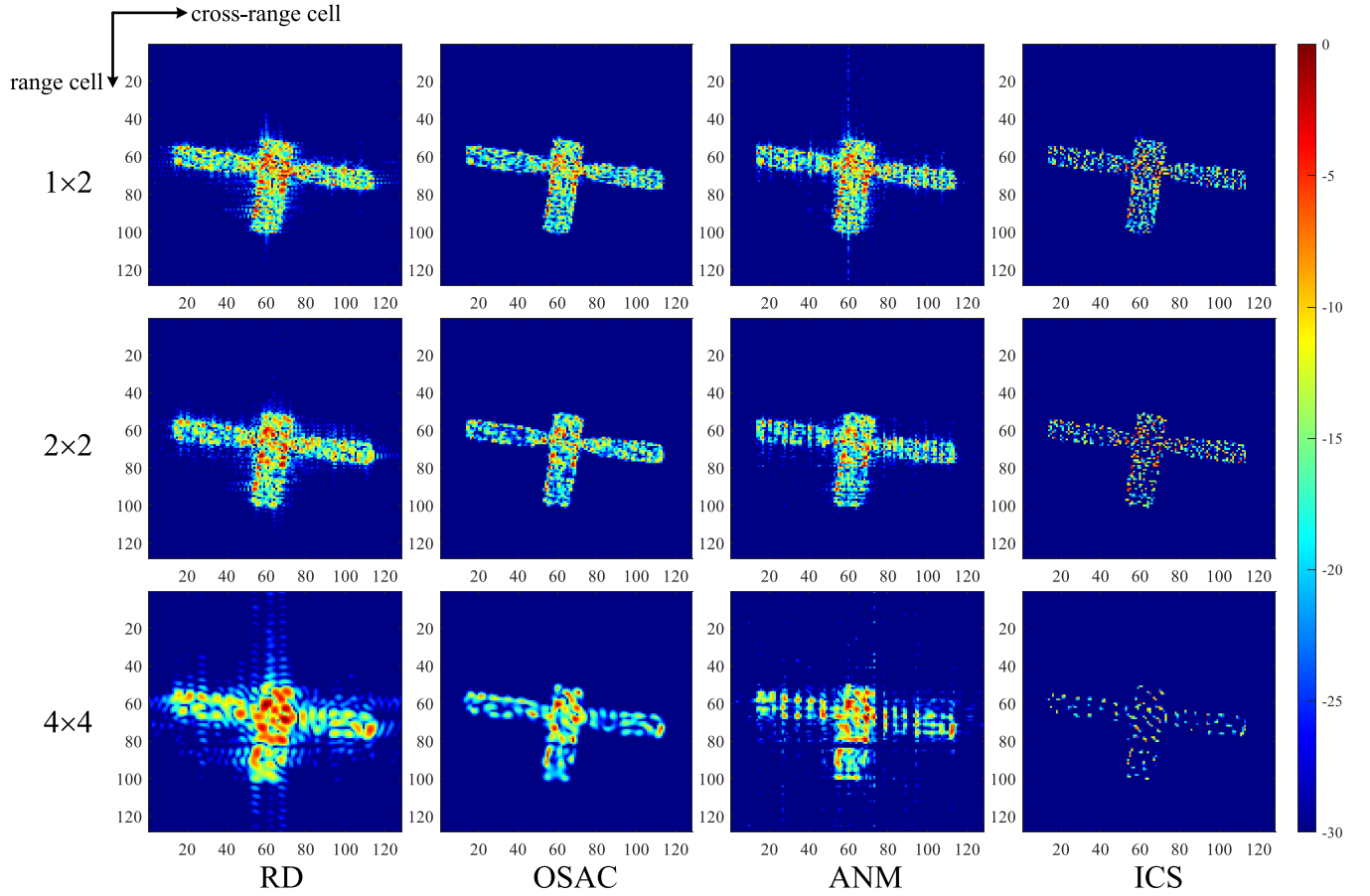


Fig. 10. Comparison of imaging results with respect to SRF. From top to bottom are results of  $\text{SRF} = 1 \times 2$ ,  $\text{SRF} = 2 \times 2$ , and  $\text{SRF} = 4 \times 4$ .

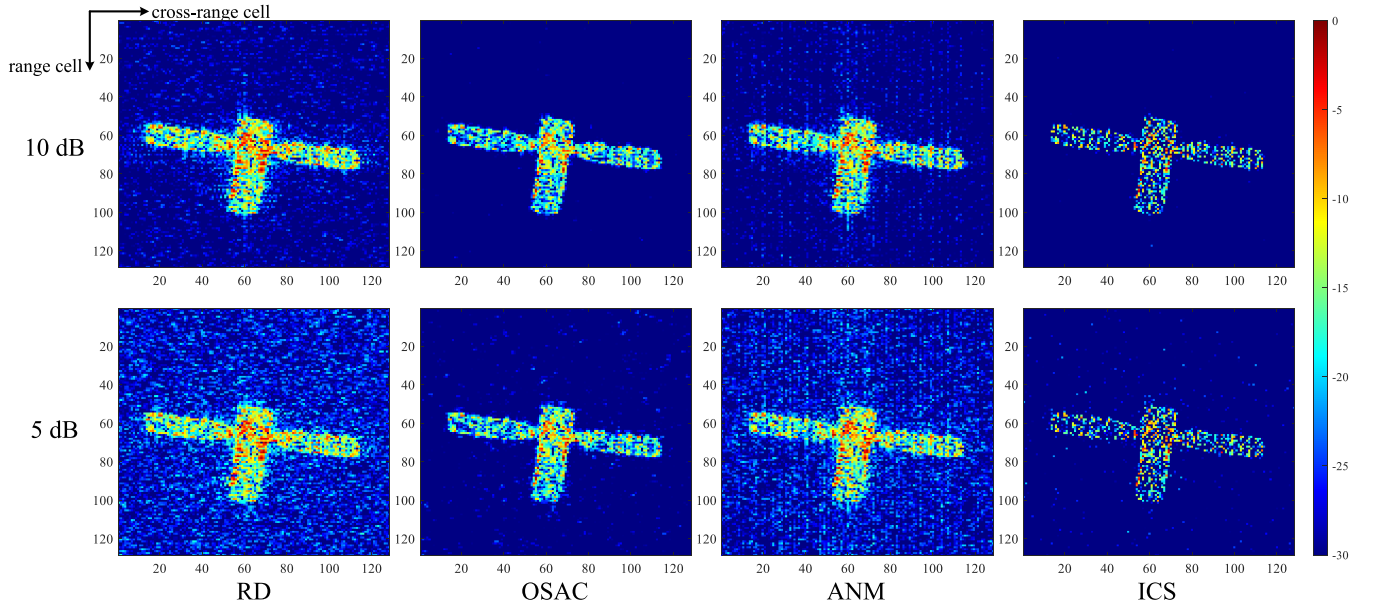


Fig. 11. Comparison of imaging results with respect to the SNR in the case of  $\text{SRF} = 1 \times 2$ . From top to bottom are the results of 10- and 5-dB SNR.

which corresponds to the theoretical resolution with  $\tilde{N}$  samples, and the exact number of samples is  $N$ , the SRF is then defined as  $\text{SRF} = \tilde{N}/N$ , which follows the definition in [9]. In the experiments of ISAR imaging, as is revealed in (14) and (15), the range resolution is proportional to the number of samples per pulse, that is,  $\delta_r \propto 1/M$ , the cross-range

resolution is proportional to the number of pulses, that is,  $\delta_a \propto 1/N$ . When the imaging result from the echo with  $\tilde{N}$  pulses and  $\tilde{M}$  samples per pulse is assumed as the expected reference image and the echo with  $N$  pulses and  $M$  samples per pulse is used for super-resolution imaging, the SRF is then defined as  $\text{SRF} = (\tilde{M}/M) \times (\tilde{N}/N)$ . Three metrics, the peak



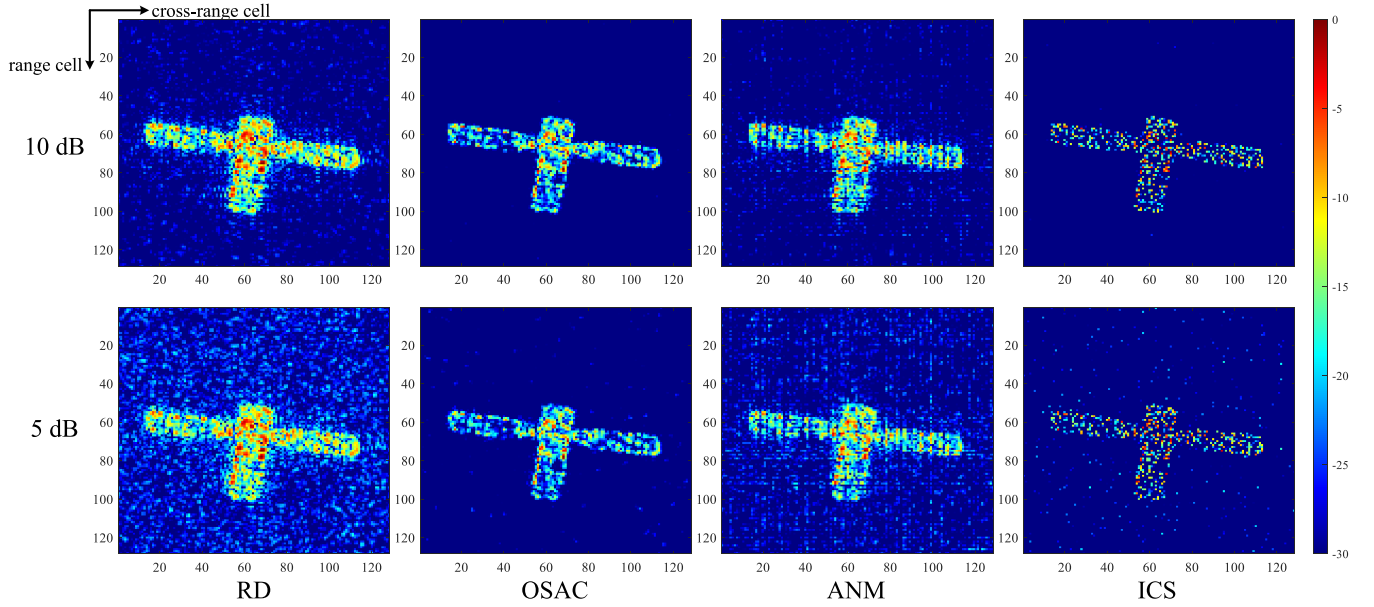


Fig. 12. Comparison of imaging results with respect to the SNR in the case of  $\text{SRF} = 2 \times 2$ . From top to bottom are the results of 10- and 5-dB SNR.

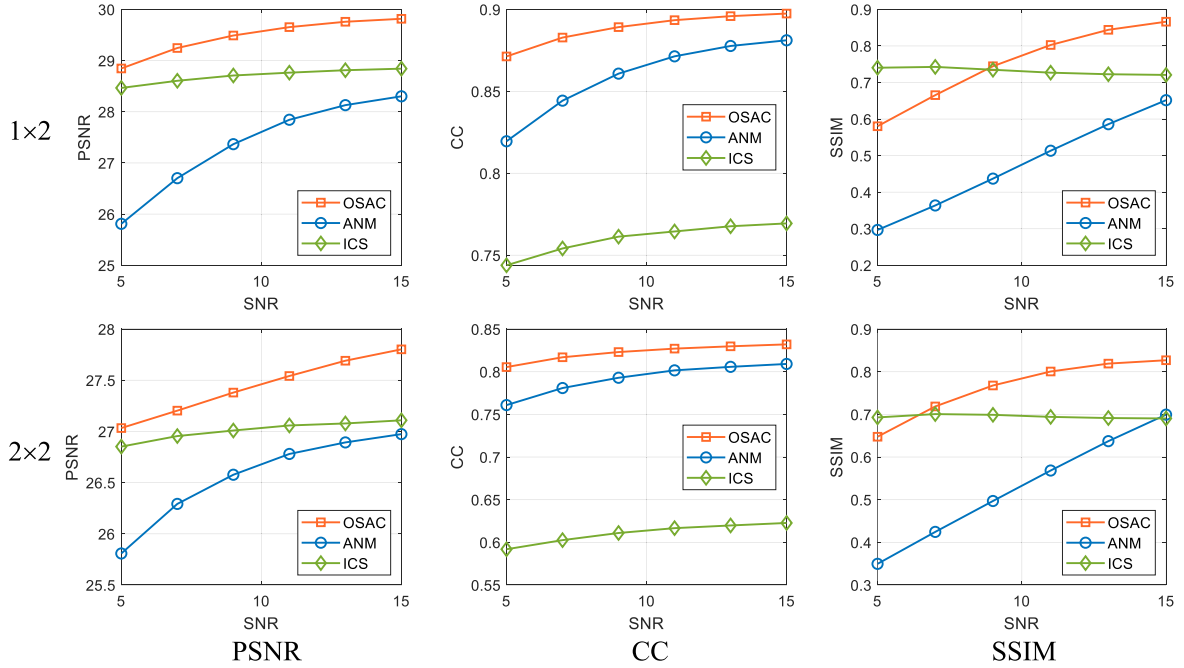


Fig. 13. Curves of metrics with respect to the SNR and SRF.

signal-to-noise ratio (PSNR), correlation coefficient (CC), and structure similarity index measure (SSIM), are used to evaluate the performance of the proposed algorithm quantitatively. For super-resolution result  $\mathbf{X}$  and reference image  $\mathbf{X}_{\text{ref}}$ , definitions of metrics are given by

$$\begin{aligned} \text{PSNR} &= 20 \log_{10} \left( \frac{\max(|\mathbf{X}|) \cdot MN}{\|\mathbf{X} - \mathbf{X}_{\text{ref}}\|_F^2} \right) \\ \text{CC} &= \frac{\sum_{m=1}^M \sum_{n=1}^N |\mathbf{X}(m, n)| \cdot |\mathbf{X}_{\text{ref}}(m, n)|}{\|\mathbf{X}\|_F \cdot \|\mathbf{X}_{\text{ref}}\|_F} \\ \text{SSIM} &= \frac{(2\mu_{\mathbf{X}}\mu_{\mathbf{X}_{\text{ref}}} + c_1)(\sigma_{\mathbf{X}\mathbf{X}_{\text{ref}}} + c_2)}{(\mu_{\mathbf{X}}^2 + \mu_{\mathbf{X}_{\text{ref}}}^2 + c_1)(\sigma_{\mathbf{X}}^2 + \sigma_{\mathbf{X}_{\text{ref}}}^2 + c_2)} \end{aligned} \quad (33)$$

where  $\mu_{\mathbf{X}}$  is the mean of  $|\mathbf{X}|$ ,  $\sigma_{\mathbf{X}}$  is the variance of  $|\mathbf{X}|$ , and  $\sigma_{\mathbf{X}\mathbf{X}_{\text{ref}}}$  is the covariance of  $|\mathbf{X}|$  and  $|\mathbf{X}_{\text{ref}}|$ .  $c_1 = (0.01L)^2$  and  $c_2 = (0.03L)^2$  and  $L$  is the dynamic range of pixel values.

It should be noted that images and corresponding echoes are normalized to 1 in the following experiments. During computation, the amplitude of the image is used. In addition, quantization was performed using a 16-bit integer format when calculating the SSIM.

#### A. Simulated Experiments of Line Spectrum Estimation

The super-resolution performance of the OSAC algorithm for line spectrum estimation of Diracs is verified in this section.

TABLE II  
KEY PARAMETERS OF THE YAK-42 AIRCRAFT DATASET

System Parameters	Value
Carrier frequency	5.52 GHz
Bandwidth	400 MHz
Pulse repetition frequency	100 Hz
Number of samples per pulse	256
Number of pulses in CPI	256

TABLE III  
KEY PARAMETERS OF THE CIVIL AIRCRAFT DATASET

System Parameters	Value
Carrier frequency	8.1 GHz
Bandwidth	800 MHz
Pulse repetition frequency	150 Hz
Number of samples per pulse	256
Number of pulses in CPI	256

First, two super-resolution cases are simulated with a fixed number of samples  $N = 32$ . In the first case, the frequencies are set as  $\{f_1, f_2, f_3\} = \{0.4961, 0.5117, 0.5977\}$ , where the spacing of two nearest Diracs corresponds to  $\text{SRF} = 2$ . In the second case, the frequencies are set as  $\{f_1, f_2, f_3\} = \{0.4961, 0.5039, 0.5977\}$ , where the spacing of two nearest Diracs corresponds to  $\text{SRF} = 4$ . In both cases, the spacing is below the resolution limit. The results of line spectrum estimation are presented in Fig. 7. As depicted, OSAC can successfully exceed the resolution limit, effectively achieving super-resolution in line spectrum estimation.

Subsequently, the success rate of super-resolution versus the signal-to-noise ratio (SNR) and the SRF is verified and shown in Fig. 8. The SRF is set as  $\text{SRF} = 2$ ,  $\text{SRF} = 8/3$ , and  $\text{SRF} = 4$ , respectively. The SNR varies from 20 to 50 dB with a step of 2 dB. Two Diracs with frequencies  $\{f_1, f_2\} = \{0.5, 0.5 + 1/N/\text{SRF}\}$  are considered in each simulation. An estimation is deemed successful if the estimated results  $\{\hat{f}_1, \hat{f}_2\}$  agree with the true values  $\{f_1, f_2\}$  with a tolerance of  $|\hat{f}_i - f_i| \leq 10^{-3}$  for  $i = 1, 2$ . A total number of 1000 Monte Carlo experiments are conducted. As Fig. 8 shows, OSAC exhibits excellent super-resolution performance at high SNR levels and demonstrates robustness against noise. When the SNR is larger than 20 dB, OSAC can achieve two times better super-resolution, that is,  $\text{SRF} = 2$ , with a success rate higher than 0.95. Under the condition that the SNR exceeds 40 dB and  $\text{SRF} = 4$ , OSAC is capable of resolving Diracs with a success rate higher than 0.95.

### B. Simulated Experiments of ISAR Imaging

Experiments on super-resolution ISAR imaging using simulated data are carried out. The data are generated from a simulated satellite target consisting of ideal scatterers with random phases. The model and the reference image for simulated experiments are shown in Fig. 9. The system parameters

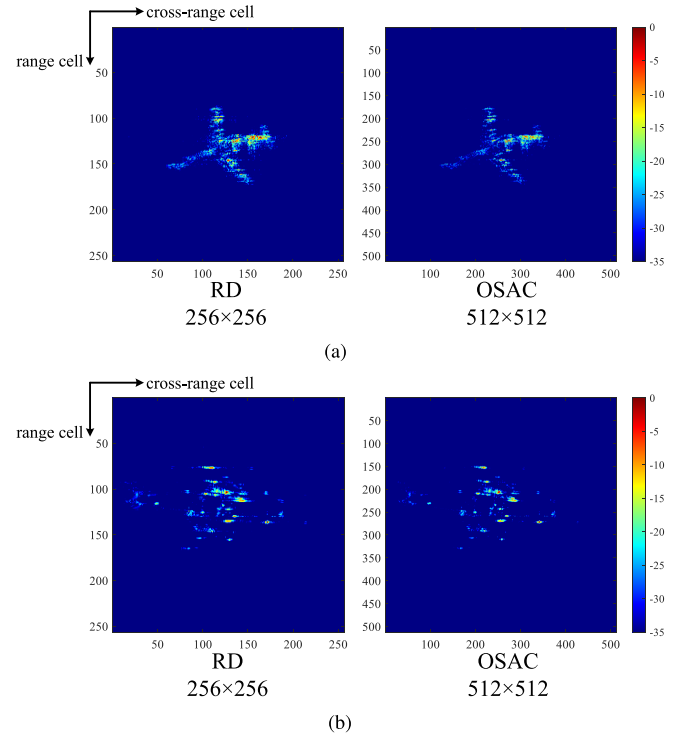


Fig. 14. Comparison of imaging results of (a) the Yak-42 aircraft and (b) civil aircraft after extrapolation on raw echo.

are given in Table I. Here, the number of pulses and the number of samples per pulse are set as  $\tilde{M} = \tilde{N} = 128$  for the expected reference image. The simulated data are ideal, devoid of any additional noise before experiments. Two cases of super-resolution imaging are considered in this section: azimuth super-resolution and joint range and azimuth super-resolution. For azimuth super-resolution, a total of 64 pulses with 128 samples per pulse are available, which corresponds to the echo with full bandwidth and half aperture, that is,  $\text{SRF} = 1 \times 2$ . In the case of joint range and azimuth super-resolution, only 64 pulses with 64 samples per pulse are available, representing the echo with half bandwidth and half aperture, that is,  $\text{SRF} = 2 \times 2$ . Furthermore, a case with 32 pulses and 32 samples per pulse is also investigated, which corresponds to the echo with a quarter of bandwidth and a quarter of aperture, that is,  $\text{SRF} = 4 \times 4$ . The imaging results across SRF and varying SNRs are discussed below.

1) *Performance Versus SRF*: The performance in relation to SRF is first assessed. A constant SNR of 20 dB is maintained for each algorithm across all cases. The super-resolution imaging results of OSAC, ANM, and ICS are shown in Fig. 10. The imaging results of the proposed algorithm closely resemble the reference image in both cases. Due to the fact that RD only performs interpolation and does not have super-resolution capability, the image quality deteriorates significantly with limited bandwidth and short aperture. ICS, as a typical super-resolution algorithm, can achieve resolution enhancement and the strong scatterers in the reconstructed image are sharpened. Qualitatively, the performance of the ANM is moderate, as it overly emphasizes the joint relationship between 2-D atoms without adequately suppressing sidelobes. The proposed OSAC algorithm preserves target information well for

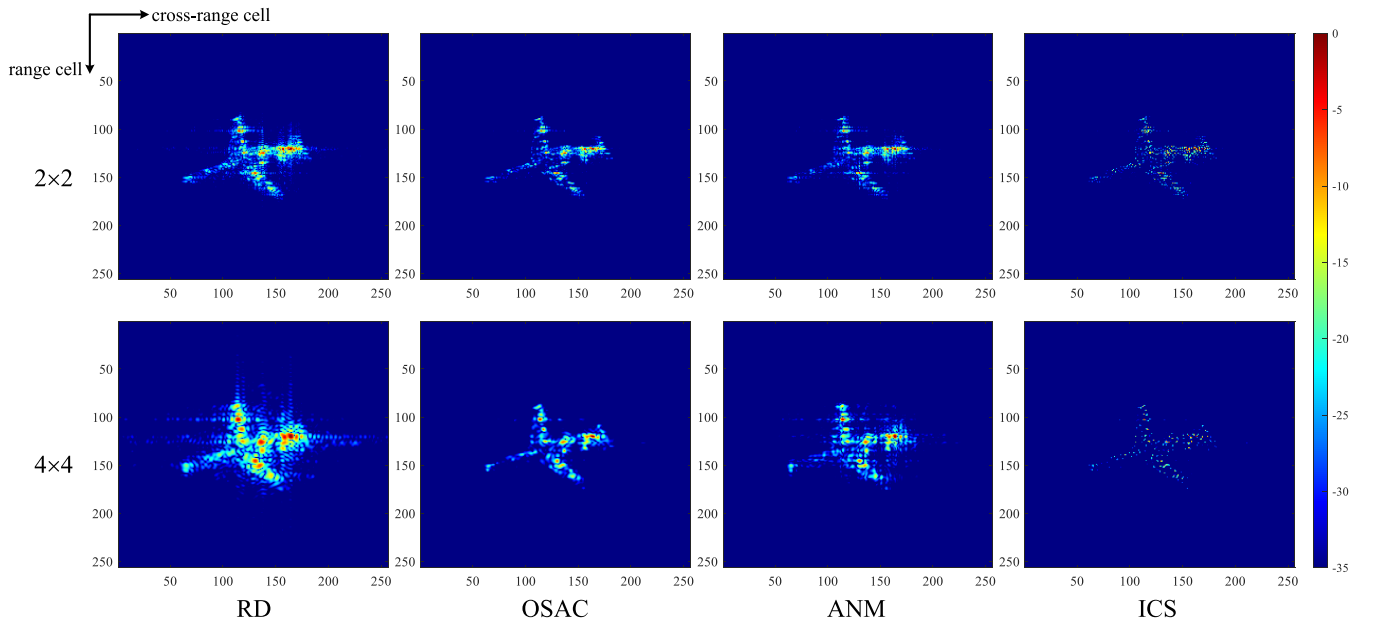


Fig. 15. Comparison of imaging results of the Yak-42 aircraft dataset in the case of  $\text{SRF} = 2 \times 2$  and  $\text{SRF} = 4 \times 4$ . From left to right are the results of RD, OSAC, ANM, and ICS.

structured targets while enhancing resolution, confirming its super-resolution ability in both cases.

2) *Performance Versus SNR*: The performance versus SNR is also evaluated in this part. The super-resolution imaging results with  $\text{SRF} = 1 \times 2$  and  $\text{SRF} = 2 \times 2$  in the case of 5- and 10-dB SNR are shown in Figs. 11 and 12, respectively. In the case of low SNR, OSAC can still achieve high-resolution imaging with limited bandwidth and variation angle. From the figure, it can be qualitatively observed that the proposed algorithm exhibits good super-resolution performance under various SNRs. Compared to other algorithms, it better preserves the structural information of the target, making it easier to extract typical components.

The metrics of PSNR, CC, and SSIM are shown in Fig. 13 to evaluate the imaging performance quantitatively. It can be seen that although ICS shows a less significant performance decline with the decrease in the SNR, it tends to lose the structure information of the target, resulting in lower CC and SSIM. The proposed OSAC algorithm has the best PSNR, CC, and SSIM in the case of a high SNR. The higher the SNR, the more significant the PSNR advantage of the proposed algorithm compared to ICS, with a maximum gain of 2 dB at  $\text{SRF} = 2 \times 2$ . When handling low SNR echo, the proposed algorithm also exhibits good robustness. Although ICS has superiority in the SSIM metric around 5-dB SNR, its CC is much lower than OSAC and ANM. Based on the two metrics of structural similarity, the imaging results of OSAC have better structural integrity than ICS.

### C. Measured Data Experiments of ISAR Imaging

The measured data experiments are carried out using the dataset of a Yak-42 aircraft and the dataset of a civil aircraft, respectively. The details of the datasets can be found in [11] and [23]. The key parameters of the Yak-42 aircraft dataset and the civil aircraft dataset are shown in Tables II and III,

respectively. Here, the number of pulses and the number of samples per pulse are set as  $\tilde{M} = \tilde{N} = 256$  for the expected reference images of both datasets. No additional noise is added on both datasets.

1) *Direct Extrapolation on Raw Echo for Qualitative Analyses*: First, the raw echoes are directly extrapolated to  $512 \times 512$  using OSAC in this part. The reference images and the results of super-resolution are depicted in Fig. 14. As shown in the figure, the imaging results of the proposed algorithm on both datasets are more precise and focused. Adjacent scattering points on the target are effectively resolved, with a narrower mainlobe and lower sidelobe level.

2) *Truncating on Raw Echo for Both Qualitative and Quantitative Analyses*: Then, the imaging results of the raw echoes are used as expected reference images and the truncated echoes are used for super-resolution imaging. The results of OSAC and other algorithms are compared in the following. Half and quarter of pulses and samples per pulse (i.e.,  $\text{SRF} = 2 \times 2$  and  $\text{SRF} = 4 \times 4$ ) are used for experiments.

The results of the Yak-42 aircraft dataset and the civil aircraft dataset are shown in Figs. 15 and 16, respectively. It can be seen from the figures that the proposed OSAC algorithm, ANM, and ICS can all achieve resolution enhancement for real measured data. Visually, the imaging performance of the ANM-based algorithm is relatively poor, while the structure information such as the outline of aircraft target in the result of  $l_1$  norm-constrained algorithm is weakened. A possible reason is that operators similar to the soft threshold are usually adopted in  $l_1$ -norm-based algorithms, making the imaging results isolated. The OSAC algorithm has the best visual performance among all the algorithms on both datasets, demonstrating its robustness to different targets.

Three metrics are also used to analyze the performance of the proposed algorithm, as shown in Table IV. The proposed algorithm has higher PSNR, CC, and SSIM in both cases of available samples on both datasets, indicating its good

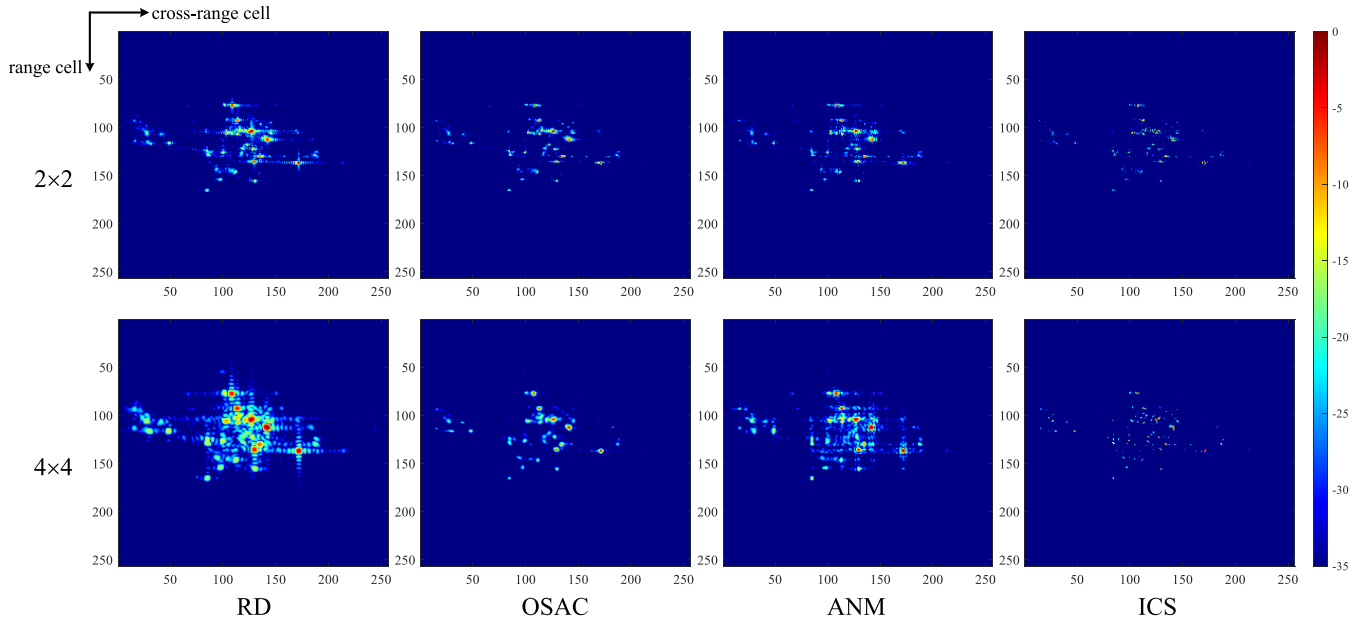


Fig. 16. Comparison of imaging results of the civil aircraft dataset in the case of  $\text{SRF} = 2 \times 2$  and  $\text{SRF} = 4 \times 4$ . From left to right are the results of RD, OSAC, ANM, and ICS.

TABLE IV  
COMPARISON OF DIFFERENT ALGORITHMS WITH RESPECT TO DIFFERENT DATASETS AND DIFFERENT SRFs

Dataset	SRF	OSAC			ANM			ICS		
		PSNR	CC	SSIM	PSNR	CC	SSIM	PSNR	CC	SSIM
The Yak-42 aircraft	$2 \times 2$	39.6761	0.8205	0.9764	39.1177	0.7948	0.9778	36.7387	0.6066	0.9448
	$4 \times 4$	36.9746	0.6828	0.9672	35.8950	0.6653	0.9412	35.0777	0.3291	0.9324
The civil aircraft	$2 \times 2$	42.3929	0.8617	0.9791	42.4279	0.8707	0.9792	40.3425	0.7419	0.9485
	$4 \times 4$	39.9895	0.7725	0.9714	36.3002	0.7627	0.9332	38.3252	0.5848	0.9408

super-resolution imaging performance. In the case of  $\text{SRF} = 2 \times 2$  using the Yak-42 aircraft dataset, the PSNR of OSAC is around 3 dB higher than ICS. That is to say, its imaging result is twice as close to the reference image of wide bandwidth and long aperture. In the case of  $\text{SRF} = 4 \times 4$ , the metrics of OSAC also show mild superiority over that of ICS. It can also be observed from CC and SSIM that the proposed algorithm has a better correlation with high-resolution reference images due to preserving the structural information of the target.

## V. CONCLUSION

In this article, a super-resolution ISAR imaging algorithm using the structured low-rank property is proposed. In the scheme, the target component is considered to be embedded in the low-dimensional subspace of high-dimensional echo. The rest called annihilating subspace is orthogonal to the corresponding target component. To estimate the annihilating subspace, a structured echo matrix is constructed based on low-resolution echo, and SVD is performed. The annihilating filter is estimated by reweighting and combining the singular vectors corresponding to the smallest singular values. Then, the annihilating property is used as a constraint for the minimization problem. Super-resolution imaging is achieved by updating the annihilating filter and the imaging result

iteratively. The proposed algorithm can achieve high-resolution ISAR imaging with limited bandwidth and short aperture.

## REFERENCES

- [1] H. Yuan, S.-Y. Zhao, Y.-J. Chen, Y. Luo, Y.-X. Liu, and Y.-P. Zhang, "Micromotion parameters estimation of precession cone based on monostatic radars," *IEEE Trans. Antennas Propag.*, vol. 72, no. 3, pp. 2811–2824, Mar. 2024, doi: [10.1109/TAP.2023.3335995](https://doi.org/10.1109/TAP.2023.3335995).
- [2] R. Li, S. Zhang, Y. Liu, and X. Li, "A sparse aperture ISAR imaging and autofocus method based on meta-learning framework," *IEEE Trans. Antennas Propag.*, vol. 72, no. 4, pp. 3529–3544, Apr. 2024, doi: [10.1109/TAP.2024.3361664](https://doi.org/10.1109/TAP.2024.3361664).
- [3] X. Lv, M. Xing, C. Wan, and S. Zhang, "ISAR imaging of maneuvering targets based on the range centroid Doppler technique," *IEEE Trans. Image Process.*, vol. 19, no. 1, pp. 141–153, Jan. 2010, doi: [10.1109/TIP.2009.2032892](https://doi.org/10.1109/TIP.2009.2032892).
- [4] H. Du, P. Ni, J. Chen, S. Ma, H. Zhang, and G. Xu, "Integrated convolution network for ISAR imaging and target recognition," *IEEE J. Miniaturization Air Space Syst.*, vol. 4, no. 4, pp. 431–437, Dec. 2023, doi: [10.1109/JMASS.2023.3325526](https://doi.org/10.1109/JMASS.2023.3325526).
- [5] Y. Zhou, L. Zhang, Y. Cao, and Y. Huang, "Optical-and-radar image fusion for dynamic estimation of spin satellites," *IEEE Trans. Image Process.*, vol. 29, pp. 2963–2976, 2020, doi: [10.1109/TIP.2019.2955248](https://doi.org/10.1109/TIP.2019.2955248).
- [6] J. A. Given and W. R. Schmidt, "Generalized ISAR—Part I: An optimal method for imaging large naval vessels," *IEEE Trans. Image Process.*, vol. 14, no. 11, pp. 1783–1791, Nov. 2005, doi: [10.1109/TIP.2005.857283](https://doi.org/10.1109/TIP.2005.857283).



- [7] J. Qian, S. Huang, L. Wang, G. Bi, and X. Yang, "Super-resolution ISAR imaging for maneuvering target based on deep-learning-assisted time-frequency analysis," *IEEE Trans. Geosci. Remote Sens.*, vol. 60, 2022, Art. no. 5201514, doi: [10.1109/TGRS.2021.3050189](https://doi.org/10.1109/TGRS.2021.3050189).
- [8] D. J. Thomson, "Spectrum estimation and harmonic analysis," *Proc. IEEE*, vol. 70, no. 9, pp. 1055–1096, Sep. 1982, doi: [10.1109/PROC.1982.12433](https://doi.org/10.1109/PROC.1982.12433).
- [9] E. J. Candès and C. Fernandez-Granda, "Towards a mathematical theory of super-resolution," *Commun. Pure Appl. Math.*, vol. 67, no. 6, pp. 906–956, 2014.
- [10] L. Zhang, M. Xing, C. -W. Qiu, J. Li, and Z. Bao, "Achieving higher resolution ISAR imaging with limited pulses via compressed sampling," *IEEE Geosci. Remote Sens. Lett.*, vol. 6, no. 3, pp. 567–571, Jul. 2009, doi: [10.1109/LGRS.2009.2021584](https://doi.org/10.1109/LGRS.2009.2021584).
- [11] L. Zhang et al., "Resolution enhancement for inversed synthetic aperture radar imaging under low SNR via improved compressive sensing," *IEEE Trans. Geosci. Remote Sens.*, vol. 48, no. 10, pp. 3824–3838, Oct. 2010, doi: [10.1109/TGRS.2010.2048575](https://doi.org/10.1109/TGRS.2010.2048575).
- [12] X. Xu and R. M. Narayanan, "Enhanced resolution in SAR/ISAR imaging using iterative sidelobe apodization," *IEEE Trans. Image Process.*, vol. 14, no. 4, pp. 537–547, Apr. 2005, doi: [10.1109/TIP.2004.841198](https://doi.org/10.1109/TIP.2004.841198).
- [13] P. Zhou, M. Martorella, X. Zhang, Y. Dai, W. Sun, and Y. Wan, "Circular scan ISAR mode super-resolution imaging of ships based on a combination of data extrapolation and compressed sensing," *IEEE Sensors J.*, vol. 19, no. 16, pp. 6883–6894, Aug. 2019, doi: [10.1109/JSEN.2019.2913903](https://doi.org/10.1109/JSEN.2019.2913903).
- [14] Y. Wang and Q. Liu, "Super-resolution sparse aperture ISAR imaging of maneuvering target via the RELAX algorithm," *IEEE Sensors J.*, vol. 18, no. 21, pp. 8726–8738, Nov. 2018, doi: [10.1109/JSEN.2018.2868308](https://doi.org/10.1109/JSEN.2018.2868308).
- [15] P. Hu, S. Xu, W. Wu, B. Tian, and Z. Chen, "IAA-based high-resolution ISAR imaging with small rotational angle," *IEEE Geosci. Remote Sens. Lett.*, vol. 14, no. 11, pp. 1978–1982, Nov. 2017, doi: [10.1109/LGRS.2017.2744989](https://doi.org/10.1109/LGRS.2017.2744989).
- [16] P. Huang et al., "High-resolution ISAR imaging for maneuvering targets based on iterative adaptive processing," *IEEE Trans. Comput. Imag.*, vol. 7, pp. 1093–1108, 2021, doi: [10.1109/TCL.2021.3116381](https://doi.org/10.1109/TCL.2021.3116381).
- [17] Q. Liu, A. Liu, Y. Wang, and H. Li, "A super-resolution sparse aperture ISAR sensors imaging algorithm via the MUSIC technique," *IEEE Trans. Geosci. Remote Sens.*, vol. 57, no. 9, pp. 7119–7134, Sep. 2019, doi: [10.1109/TGRS.2019.2911686](https://doi.org/10.1109/TGRS.2019.2911686).
- [18] J.-H. Bae, B.-S. Kang, K.-T. Kim, and E. Yang, "Performance of sparse recovery algorithms for the reconstruction of radar images from incomplete RCS data," *IEEE Geosci. Remote Sens. Lett.*, vol. 12, no. 4, pp. 860–864, Apr. 2015, doi: [10.1109/LGRS.2014.2364601](https://doi.org/10.1109/LGRS.2014.2364601).
- [19] S. Shao, L. Zhang, J. Wei, and H. Liu, "Two-dimension joint super-resolution ISAR imaging with joint motion compensation and azimuth scaling," *IEEE Geosci. Remote Sens. Lett.*, vol. 18, no. 8, pp. 1411–1415, Aug. 2021, doi: [10.1109/LGRS.2020.3003578](https://doi.org/10.1109/LGRS.2020.3003578).
- [20] S. Shao, H. Liu, L. Zhang, P. Wang, and J. Wei, "Integration of super-resolution ISAR imaging and fine motion compensation for complex maneuvering ship targets under high sea state," *IEEE Trans. Geosci. Remote Sens.*, vol. 60, 2022, Art. no. 5222820, doi: [10.1109/TGRS.2022.3147266](https://doi.org/10.1109/TGRS.2022.3147266).
- [21] Y. Wu, S. Zhang, H. Kang, and T. S. Yeo, "Fast marginalized sparse Bayesian learning for 3-D interferometric ISAR image formation via super-resolution ISAR imaging," *IEEE J. Sel. Topics Appl. Earth Observ. Remote Sens.*, vol. 8, no. 10, pp. 4942–4951, Oct. 2015, doi: [10.1109/JSTARS.2015.2455508](https://doi.org/10.1109/JSTARS.2015.2455508).
- [22] G. Xu et al., "High-resolution mmWave SAR imagery for automotive parking assistance," *IEEE J. Miniaturization Air Space Syst.*, vol. 4, no. 1, pp. 54–61, Mar. 2023, doi: [10.1109/JMASS.2022.3226771](https://doi.org/10.1109/JMASS.2022.3226771).
- [23] G. Xu, M. Xing, X.-G. Xia, L. Zhang, Q. Chen, and Z. Bao, "3D geometry and motion estimations of maneuvering targets for interferometric ISAR with sparse aperture," *IEEE Trans. Image Process.*, vol. 25, no. 5, pp. 2005–2020, May 2016, doi: [10.1109/TIP.2016.2535362](https://doi.org/10.1109/TIP.2016.2535362).
- [24] L. Wang, L. Zhao, G. Bi, C. Wan, and L. Yang, "Enhanced ISAR imaging by exploiting the continuity of the target scene," *IEEE Trans. Geosci. Remote Sens.*, vol. 52, no. 9, pp. 5736–5750, Sep. 2014, doi: [10.1109/TGRS.2013.2292074](https://doi.org/10.1109/TGRS.2013.2292074).
- [25] H. Duan, L. Zhang, J. Fang, L. Huang, and H. Li, "Pattern-coupled sparse Bayesian learning for inverse synthetic aperture radar imaging," *IEEE Signal Process. Lett.*, vol. 22, no. 11, pp. 1995–1999, Nov. 2015, doi: [10.1109/LSP.2015.2452412](https://doi.org/10.1109/LSP.2015.2452412).
- [26] J. Fang, L. Zhang, and H. Li, "Two-dimensional pattern-coupled sparse Bayesian learning via generalized approximate message passing," *IEEE Trans. Image Process.*, vol. 25, no. 6, pp. 2920–2930, Jun. 2016, doi: [10.1109/TIP.2016.2556582](https://doi.org/10.1109/TIP.2016.2556582).
- [27] R. Li, S. Zhang, C. Zhang, Y. Liu, and X. Li, "A computational efficient 2-D block-sparse ISAR imaging method based on PCSBL-GAMP-Net," *IEEE Trans. Geosci. Remote Sens.*, vol. 60, 2022, Art. no. 5214814, doi: [10.1109/TGRS.2021.3111901](https://doi.org/10.1109/TGRS.2021.3111901).
- [28] L. Wang, L. Zhao, G. Bi, and C. Wan, "Sparse representation-based ISAR imaging using Markov random fields," *IEEE J. Sel. Topics Appl. Earth Observ. Remote Sens.*, vol. 8, no. 8, pp. 3941–3953, Aug. 2015, doi: [10.1109/JSTARS.2014.2359250](https://doi.org/10.1109/JSTARS.2014.2359250).
- [29] S. Zhang, Y. Liu, X. Li, and D. Hu, "Enhancing ISAR image efficiently via convolutional reweighted  $l_1$  minimization," *IEEE Trans. Image Process.*, vol. 30, pp. 4291–4304, 2021, doi: [10.1109/TIP.2021.3070442](https://doi.org/10.1109/TIP.2021.3070442).
- [30] Y. Yang, S. Gui, and Q. Wan, "ISAR moving target imaging method using hy-ADMM and mm-GLRT," *IEEE Sensors J.*, vol. 22, no. 3, pp. 2618–2629, Feb. 2022, doi: [10.1109/JSEN.2021.3138891](https://doi.org/10.1109/JSEN.2021.3138891).
- [31] B. Zhang, G. Xu, H. Yu, H. Wang, H. Pei, and W. Hong, "Array 3-D SAR tomography using robust gridless compressed sensing," *IEEE Trans. Geosci. Remote Sens.*, vol. 61, 2023, Art. no. 5205013, doi: [10.1109/TGRS.2023.3259980](https://doi.org/10.1109/TGRS.2023.3259980).
- [32] G. Xu, Y. Chen, A. Ji, B. Zhang, C. Yu, and W. Hong, "3-D high-resolution imaging and array calibration of ground-based millimeter-wave MIMO radar," *IEEE Trans. Microw. Theory Techn.*, vol. 72, no. 8, pp. 4919–4931, Aug. 2024, doi: [10.1109/TMTT.2024.3352406](https://doi.org/10.1109/TMTT.2024.3352406).
- [33] W. Qiu, J. Zhou, and Q. Fu, "Jointly using low-rank and sparsity priors for sparse inverse synthetic aperture radar imaging," *IEEE Trans. Image Process.*, vol. 29, pp. 100–115, 2020, doi: [10.1109/TIP.2019.2927458](https://doi.org/10.1109/TIP.2019.2927458).
- [34] G. Xu, B. Zhang, H. Yu, J. Chen, M. Xing, and W. Hong, "Sparse synthetic aperture radar imaging from compressed sensing and machine learning: Theories, applications, and trends," *IEEE Geosci. Remote Sens. Mag.*, vol. 10, no. 4, pp. 32–69, Dec. 2022, doi: [10.1109/MGRS.2022.3218801](https://doi.org/10.1109/MGRS.2022.3218801).
- [35] L. Mingjiu, W. Chen, J. Ma, J. Yang, Q. Cheng, and X. Ma, "Gridless sparse ISAR imaging via 2-D fast reweighted atomic norm minimization," *IEEE Geosci. Remote Sens. Lett.*, vol. 19, 2022, Art. no. 4025605, doi: [10.1109/LGRS.2022.3191394](https://doi.org/10.1109/LGRS.2022.3191394).
- [36] M. Vetterli, P. Marziliano, and T. Blu, "Sampling signals with finite rate of innovation," *IEEE Trans. Signal Process.*, vol. 50, no. 6, pp. 1417–1428, Jun. 2002, doi: [10.1109/TSP.2002.1003065](https://doi.org/10.1109/TSP.2002.1003065).
- [37] J. C. Ye, J. M. Kim, K. H. Jin, and K. Lee, "Compressive sampling using annihilating filter-based low-rank interpolation," *IEEE Trans. Inf. Theory*, vol. 63, no. 2, pp. 777–801, Feb. 2017, doi: [10.1109/TIT.2016.2629078](https://doi.org/10.1109/TIT.2016.2629078).
- [38] G. Ongie, S. Biswas, and M. Jacob, "Convex recovery of continuous domain piecewise constant images from nonuniform Fourier samples," *IEEE Trans. Signal Process.*, vol. 66, no. 1, pp. 236–250, Jan. 2018, doi: [10.1109/TSP.2017.2750111](https://doi.org/10.1109/TSP.2017.2750111).
- [39] J. Wang and D. Kasilingam, "Global range alignment for ISAR," *IEEE Trans. Aerosp. Electron. Syst.*, vol. 39, no. 1, pp. 351–357, Jan. 2003, doi: [10.1109/TAES.2003.1188917](https://doi.org/10.1109/TAES.2003.1188917).



**Bangjie Zhang** (Student Member, IEEE) was born in Suzhou, China, in 1995. He received the B.S. degree in information engineering from Southeast University, Nanjing, China, in 2018, where he is currently pursuing the Ph.D. degree with the State Key Laboratory of Millimeter Waves.

His research interests include millimeter-wave radar systems, SAR, and ISAR imaging.



**Gang Xu** (Senior Member, IEEE) was born in Zaozhuang, China, in 1987. He received the B.S. and Ph.D. degrees in electrical engineering from Xidian University, Xi'an, China, in 2009 and 2015, respectively.

From 2015 to 2016, he was a full-time Post-Doctoral Research Fellow with the School of Electrical and Electronic Engineering, Nanyang Technological University, Singapore. He is currently a Professor with the State Key Laboratory of Millimeter Waves, School of Information Science and Engineering, Southeast University, Nanjing, China. His research interests include SAR/ISAR imaging and millimeter-wave radar.



**Xiang-Gen Xia** (Fellow, IEEE) received the B.S. degree in mathematics from Nanjing Normal University, Nanjing, China, in 1983, the M.S. degree in mathematics from Nankai University, Tianjin, China, in 1986, and the Ph.D. degree in electrical engineering from the University of Southern California, Los Angeles, CA, USA, in 1992.

He was a Senior/Research Staff Member with Hughes Research Laboratories, Malibu, CA, USA, from 1995 to 1996. In September 1996, he joined the Department of Electrical and Computer Engineering, University of Delaware, Newark, DE, USA, where he is currently the Charles Black Evans Professor. He is the author of the book *Modulated Coding for Intersymbol Interference Channels* (New York, Marcel Dekker, 2000) and a co-author of the book *Array Beamforming Enabled Wireless Communications* (New York, CRC Press, 2023). His current research interests include space-time coding, MIMO and OFDM systems, digital signal processing, and SAR and ISAR imaging.

Dr. Xia received the National Science Foundation (NSF) Faculty Early Career Development (CAREER) Program Award in 1997, the Office of Naval Research (ONR) Young Investigator Award in 1998, and the Outstanding Overseas Young Investigator Award from the National Nature Science Foundation of China in 2001. He received the 2019 Information Theory Outstanding Overseas Chinese Scientist Award, The Information Theory Society of the Chinese Institute of Electronics. He is the Technical Program Chair of the Signal Processing Symposium, Globecom 2007, in Washington, DC, USA, and the General Co-Chair of ICASSP 2005 in Philadelphia, PA, USA. He has served as an Associate Editor for numerous international journals including IEEE TRANSACTIONS ON SIGNAL PROCESSING, IEEE TRANSACTIONS ON WIRELESS COMMUNICATIONS, IEEE TRANSACTIONS ON MOBILE COMPUTING, and IEEE TRANSACTIONS ON VEHICULAR TECHNOLOGY.



**Hanwen Yu** (Senior Member, IEEE) received the B.S. and Ph.D. degrees from Xidian University, Xi'an, China, in 2007 and 2012, respectively.

He was a Post-Doctoral Fellow with the Department of Civil and Environmental Engineering and the National Center for Airborne Laser Mapping, University of Houston, Houston, TX, USA. He is currently a Full Professor with the School of Resources and Environment, University of Electronic Science and Technology of China, Chengdu, China. He is the Adjunct Full Professor with the

Academy of Advanced Interdisciplinary Research, Xidian University, and is the Adjunct Full Professor with the Department of Engineering, University of Napoli Parthenope, Naples, Italy. He has authored more than 60 scientific articles and given a scientific presentation about "Advanced techniques in InSAR Phase Unwrapping" invited by the IEEE GRSS Webinar in 2021. He has reviewed more than 280 manuscripts for over 20 different journals. His research focuses on InSAR, and this work has led to new insights into worldwide deformation monitoring and topographic mapping.

Dr. Yu was elected as an IEEE GRSS AdCom Member beginning in 2023. He was also elected as a Best Reviewer of IEEE TRANSACTIONS ON GEOSCIENCE AND REMOTE SENSING in 2019. He has been deeply involved in IEEE (in general) and IEEE GRSS in particular. He was a recipient of several awards and honors from IEEE GRSS, including the 2021 Transactions Prize Paper Award. He was the Technical Program Committee Member and Session Chair of 2022 IGARSS and the Co-PI of the IEEE GRSS 50%-funding project "West China Initiative." He is the Editor-in-chief of IEEE JOURNAL OF MINIATURIZATION FOR AIR AND SPACE SYSTEMS, a Topical Associate Editor of IEEE TRANSACTIONS ON GEOSCIENCE AND REMOTE SENSING, and an Associate Editor of *IEEE Geoscience and Remote Sensing Magazine*.



**Mengdao Xing** (Fellow, IEEE) received the B.S. and Ph.D. degrees from Xidian University, Xian, China, in 1997 and 2002, respectively.

He is currently a Professor with the National Laboratory of Radar Signal Processing, Xidian University. He holds the appointment of the Dean with the Academy of Advanced Interdisciplinary Research Department, Xidian University. He has written or co-written more than 200 refereed scientific journal articles. He also has authored or co-authored two books about synthetic aperture radar (SAR) signal processing. The total citation times of his research are greater than 10000 (H-index 50). He was rated as a Most Cited Chinese Researcher by Elsevier. He has achieved more than 50 authorized China patents. His research has been supported by various funding programs, such as the National Science Fund for Distinguished Young Scholars. His research interests include SAR, interferometric SAR, inversed SAR, sparse signal processing, and microwave remote sensing.

Dr. Xing has guest edited several special issues in *IEEE Geoscience and Remote Sensing Magazine* and *IEEE JOURNAL OF SELECTED TOPICS IN APPLIED EARTH OBSERVATIONS AND REMOTE SENSING*. He currently serves as the Associate Editor for radar remote sensing of IEEE TRANSACTIONS ON GEOSCIENCE AND REMOTE SENSING and the Editor-in-Chief for MDPI *Sensors*.



**Wei Hong** (Fellow, IEEE) received the B.S. degree in radio engineering from the University of Information Engineering, Zhengzhou, China, in 1982, and the M.S. and Ph.D. degrees in radio engineering from Southeast University, Nanjing, China, in 1985 and 1988, respectively.

Since 1988, he has been with the State Key Laboratory of Millimeter Waves, Southeast University, where he has been the Director since 2003. In 1993, he joined the University of California at Berkeley, Berkeley, CA, USA, as a Short-Term Visiting Scholar. From 1995 to 1998, he was a Short-Term Visiting Scholar with the University of California at Santa Cruz, Santa Cruz, CA, USA. He is currently a Professor with the School of Information Science and Engineering, Southeast University. He has authored or co-authored over 300 technical publications and authored two books. His current research interests include numerical methods for electromagnetic problems, millimeter-wave theory and technology, antennas, electromagnetic scattering, and RF technology for mobile communications.

Dr. Hong was an Elected IEEE MTT-S AdCom Member from 2014 to 2016. He is a fellow of CIE. He was a recipient of the National Natural Prizes twice, the First-Class Science and Technology Progress Prizes thrice, issued by the Ministry of Education of China and Jiangsu Province Government, and the Foundations for China Distinguished Young Investigators and "Innovation Group" issued by the NSF of China. He is currently a Vice President of the CIE Microwave Society and Antenna Society and the Chair of the IEEE MTT-S/APS/EMCS Joint Nanjing Chapter. He served as an Associate Editor for IEEE TRANSACTIONS ON MICROWAVE THEORY AND TECHNIQUES from 2007 to 2010 and one of the Guest Editors for the 5G Special Issue of IEEE TRANSACTIONS ON ANTENNAS AND PROPAGATION in 2017.